Topological mechanical metamaterial for robust and ductile one-way fracturing

Xinyu Wang
University of Michigan https://orcid.org/0009-0000-4370-2174
Siddhartha Sarkar
University of Michigan
Stefano Gonella
University of Minnesota https://orcid.org/0000-0003-3705-1808
Xiaoming Mao
maox@umich.edu
University of Michigan https://orcid.org/0000-0001-7920-3991

Research Article

Keywords: topological mechanics, one-way fracturing, linear elastic fracture mechanics, mechanical metamaterials

Posted Date: December 20th, 2024

DOI: https://doi.org/10.21203/rs.3.rs-5677605/v1

Additional Declarations: The authors declare no competing interests.

Topological mechanical metamaterial for robust and ductile one-way fracturing

Xinyu Wang[1], Siddhartha Sarkar[1], Stefano Gonella[2], Xiaoming Mao[1*]
[1]Department of Physics, University of Michigan, Ann Arbor, MI 48109, USA
[2]Department of Civil, Environmental, and Geo- Engineering, University of Minnesota, Minneapolis, MN 55455, USA
* Corresponding author: maox@umich.edu

November 4, 2024

Abstract

Fracturing is unavoidable and threatens the reliability and functionality of materials. Therefore, regulating the propagation of cracks in a predictable and ductile manner is of paramount importance. Herein, we exploit the properties of topological mechanical metamaterials (TMMs) as a versatile mechanism to guide cracks unidirectionally and turn fracturing of lattices made of brittle materials into ductile events. Inspired by quantum topological states, recent discoveries of TMMs have uncovered varieties of unconventional mechanical phenomena, ranging from one-way wave propagation to polar elasticity. We show that polarized floppy modes occurring in TMMs lead to strongly asymmetric stress fields localizing around the crack tips, leading to ductile one-way fracturing, in sharp contrast to classical theories of fractures in brittle materials. Our work demonstrates the universality of this fracture unidirectionality feature, which is protected by TMM's bulk topology, and provides robust solutions in programmable fracturing for a broad class of materials and structures.

Keywords— topological mechanics, one-way fracturing, linear elastic fracture mechanics, mechanical metamaterials

1 Introduction

Fracture undermines the stability of structural and material systems across scales and physical realms, from rocks [1], bones and teeth [2, 3], polymers [4, 5, 6, 7, 8, 9, 10, 11, 12], to two-dimensional materials [13, 14, 15] and microscale molecules and fibers [16, 17, 18, 19]. Fractures are inevitable; what one can do is design materials endowed with the ability to retard the manifestation of fracturing (crack initiation and propagation) or mitigate the severity of fracturing events to avoid the onset of catastrophic damage. To this end, understanding and subsequently controlling the parameters that guide fracture propagation remains a key challenge in theoretical and practical research in fracture mechanics [20, 21, 22, 23, 24, 25, 26, 27, 28, 29, 30, 31, 32]. Recently proposed methods to steer cracking direction includes applying different external loading conditions [33, 34, 23, 35], controlling material anisotropy (e.g., using bio-inspired nacre [36] and seashell [37]), programming the micro-structure geometry [38, 39, 40, 41] and introducing local curvature [42, 43]. Despite this abundance of approaches, a robust general principle for using geometry to guide the direction of fractures is still lacking.

In the past decade, principles from quantum topological states of matter have been widely utilized to design mechanical metamaterials featuring topologically protected properties, such as one-way edge states and polarized elasticity [44, 45, 46, 47, 48]. Among them, Maxwell lattices have attracted extensive interest due to the ability to topologically control stress and strain fields, offering programmable soft boundaries [44, 49, 50, 51], transformable responses [52, 53, 54], programmable stress distribution [55, 56, 57, 58], and low-frequency edge waves [59, 60].

In this paper, we show that topological mechanics of Maxwell lattices can be used to robustly guide fractures to propagate in a unidirectional and sequential way, and we demonstrate this effect using theories, simulations and experiments. We find that the topological polarization, which controls the spatial patterns of the stress fields and specifically the regions of stress focusing, is responsible for strong asymmetries in the stress fields that localize around cracks, causing the lattice to fracture along a deterministic and predictable direction. Remarkably, this property is preserved even when the fracture progresses into the nonlinear regime. Moreover, the sequential activation of topological zero modes resulting from the onset of crack make the fracture process ductile, although the material the lattice is made from is brittle. Such geometry-induced effective ductility drastically reduces the occurrence of catastrophic failures. We provide rationales for our results in light of topologically protected zero modes (ZMs) in Maxwell TMMs, and compare our results with linear elastic fracture mechanics (LEFM) [61, 62, 63, 64]. Specifically, we find that topological ZMs generates stress distributions that significantly differ from those predicted by LEFM in terms of both asymmetries and angular profiles near the crack tip, thus providing drivers for crack propagation that differ qualitatively by those observed in classical media as well as in non-polarized lattices.

In summary, the properties of TMMs enable several advances in fracture mechanics and engineering: (1) using the combination of purely periodic geometry and isotropic constituent materials, the cracks are guided in a unidirectional and robust way even in the nonlinear regime, *regardless of the crack shape*; (2) the TMM turns a sudden, brittle and unpredictable failure into a *ductile and predictable* one with early indicators; (3) the TMM enables *on-demand control of crack tip stress conditions* and achieves diffusive and concentrated fracturing in the same material; (4) based on topological kagome lattices, the TMM is light-weighted and features material-invariant and scale-invariant properties.

This study also aims at filling important gaps in efforts to apply TMMs to real-world engineering problems. The mechanics of Maxwell lattices have been primarily studied in the context of ideal spring-mass models. How topological mechanical effects manifest in structural lattices that can be fabricated via realistic manufacturing methods is a rich and on-going question. So far, several studies have pinpointed the signature of structural non-ideality to a general dilution of the topological polarization, accompanied by the rising of the characteristic spectra of the topological modes to finite frequencies [59, 65, 60]. On the other hand, working with structural lattices poses additional opportunities, e.g., for tuning of transformable lattice using external stimuli [54]. As for the effects of structural dilution on the stability and failure of TMMs, recent works have documented a substantial robustness of topologically protected stress focusing in structural lattices [57], which is only compromised in regimes of large deformation [58]. However, these studies have mostly addressed the states of stress that may be precursors of crack initiation, while how the actual crack propagation conditions are affected by the polarization of TMMs is, until now, essentially uncharted. The results in this work provide a first set of answers to this question, while revealing some unexpected damage propagation regime that elude common fracture mechanics wisdom.

2 Results

2.1 Fracture of Maxwell lattice TMMs

In a homogeneous material, stress fields focus at the two tips of a crack symmetrically (Fig. 1A) [66]. As a result, in practical scenarios involving brittle materials (Fig. S1, the propagation direction (to the left or to the right) that the crack eventually follows is highly sensitive to the material's defects or imperfections and thus hard to predict or control. Moreover, the damage process is sudden and often without significant prior deformation (Movie S1). The aim of crack-guiding functional materials [35, 39, 38] is to break symmetry of the geometry and guide the crack propagation in a unidirectional and predictable way.

A trivial approach to breaking this symmetry could be obtained by modulating material constants or disrupting mirror symmetry in micro-geometry. Such approaches suffer from material and strain dependence. Here, in contrast, we explore the architecture of polarized Maxwell lattice-based TMMs (Fig. 1B) as a means to manipulate the stress field and direct the crack propagation in a robust way based on topological protection. Maxwell lattices are mechanical lattices with an equal number of degrees of freedom and constraints in the bulk, thus operating on the verge of mechanical instability. They are known to exhibit topologically polarized elasticity, which manifests as the localization of states of self stress (SSS) and zero modes (ZMs) at opposite edges of a finite lattice domain [44, 49, 50, 51].

Topologically polarized elasticity predicts that, by replacing a solid continuum (Fig. 1A) with a TMM (Fig. 1B), an asymmetric stress field emerges in the neighborhood of a crack. Note that, in a lattice, a crack effectively consists of a sequence of severed ligaments (serving as structural hinges) along a line. This scenario is depicted in Fig. 1B via FEM simulations and experimental data. For the experiment, we cut a Polyethylenimine (PEI) film into the TMM geometry in Fig. 1B and sandwich it between a pair of polarizers (see Materials and Methods, Fig. S2). After subjecting it to slight stretching, it reveals an asymmetric stress field, indicated by the color map.

We compare (1) a continuum medium (Fig. 1A) with a slim crack, (2) a topological kagome lattice TMM (Fig. 1B) and (3) a regular kagome lattice (Fig. S3) - the latter two cases featuring a line of severed hinges acting as crack. Applying the same amount of total stress to all configurations, we extract stress profiles along horizontal paths between the immediate neighborhood of the crack tips and the free boundaries (Fig. S4). For the two lattice configurations, we adopt the average von Mises stress in the structural hinges as a stress indicator (Materials and Methods). Among the three, only the topological kagome shows a strongly asymmetric stress field about the crack. (1) For the continuum medium, the stress decays as $1/\sqrt{r}$, where r is the distance from the crack tip (gray curve in Fig. 1C), consistent with classical theories [61, 62, 63, 64]. (2) For the TMM (green curve), interestingly, the left side of the crack does not display a stress build-up at the effective crack tip, while on the right side the tip stress is three times the bulk value. The fluctuations at the left edge are a signature of the floppy modes available on that open edge due to polarization. The deformation mode in the bulk is a combination of stretching and bending of the hinges. (3) For the regular kagome (orange curve), an increase of stress from the bulk to the crack tip is observed, albeit smoother than in the continuum medium and the right side of topological kagome (Fig. S5), which can be explained by the blunting effect of kagome lattices [67, 68]. For this lattice, the dominant deformation mode in the bulk is stretching. (see additional simulations in Fig. S5). In addition, the sudden drop of the stress near the boundaries (Fig. S5 C) [67] can be explained by noting that, at a free boundary, due to the lack of constraints, the deformation mode switches locally to bending-dominated and exhibits the deepest boundary layer of the three cases.

We further show that the trend of asymmetric tip stresses in TMMs continues deep into the nonlinear regime, beyond the linear elastic states of stress considered in previous studies [55, 56, 57], injecting asymmetry into the actual damage propagation regime. We test several samples for each medium type (continuum, regular kagome and TMM) featuring the same length, width, and crack size to extract some statistics of failure (Fig. 1D) and document the existence or lack thereof of crack propagation directionality in these systems. Specifically, we count the number of instances where the crack propagates left/right. As shown in Fig. 1D, when it comes to realistic experimental conditions, for the continuum medium and the regular kagome it is impossible to predict (or enforce) a priori which way the crack will propagate or induce symmetric, simultaneous, two-way propagation from both tips of the crack. This is despite the fact that they both show perfectly symmetric stress fields in simulations (Fig. 1C). In Fig. 1E, we report normalized experimental force-displacement curves acquired during the tests (see also Fig. S6). The curve for the continuum samples (grey line) clearly shows a sharp drop from the peak state, representative of canonical brittle behavior. An intermediate and final cracked state of a continuum sample are shown in Fig. 1G, and H, respectively. The paper sample undergoes infinitesimal deformation before undergoing sudden failure (Movie S1), and the direction of crack propagation is unpredictable from one sample to the next.

In contrast, the TMM presents a much slower manifestation of failure reminiscent of ductile failure, as indicated by the green line in Fig. 1E, which features a jagged profile that stretches the failure process over an elongation range 5-6 times larger than that observed for the continuum. Moreover, driven by the significant stress difference between the two tips (Fig. 1C), the crack propagates consistently to the right, as indicated by the 100% case count in Fig. 1D. The local physical processes involved in crack opening for the TMM are documented in the snapshots of Fig. 1I-M. Interestingly, before cracking, the TMM gives a warning: in both simulations and experiments, the circled right tip hinge (brown circle) shows an opening angle larger than the others by $\approx 10^\circ$ (Fig. 1I). The breaking of the first hinge on the right side corresponds to the first drop in the jagged force profile of Fig. 1E. At 203 s, with the first hinge broken, the largest stress is found in the second right tip hinge (circled), as shown in Fig. 1J. After that, the crack keeps propagating to the right, reaching the state of Fig. 1K at 333 s, with the second hinge broken and the largest stress found in the third hinge, and that of Fig. 1K at 600 s, when the one-way cracking pattern is fully formed. The final state shown in Fig. 1M at 1300 s marks the collapse point where the sample looses integrity. Inspection of the deformation and stress fields revels something additional about the mechanics of the process. As the first hinge breaks and the second one carries the largest stress, it experiences a more pronounced bending deformation, which is accompanied by an increase in stiffness (Fig. 1E, I-L). When the second hinge goes to the maximum allowed strain and breaks, we observe stress concentration in the third hinge on the right *at larger strain*. This nonlinear phenomenon is due to the sequential activation of topological ZMs in the nonlinear regime, as we discuss in the next section.

In summary, we observe systematically across the experiments that all the right side hinges are broken sequentially before the cracking transitions to the left (Fig. 1, Movie S2). Therefore, the crack propagation in the TMM can be considered *predictable, unidirectional and ductile*. Note that all simulations of TMMs are consistent with the experiments (Fig. 1I-M).

For completeness, we close this section with a few comments about the somewhat erratic behavior of the regular kagome. Here, two-way symmetric propagation is observed in the ideal simulations (Movie S3) giving rise to brittle failure (Fig. S6C). Experimentally, however, since the tip stress is blunted (Fig. 1C, Fig. 3B), the crack path is rather unpredictable and may even steer towards other directions, due to uncontrollable imperfections in the sample (Movie S4). This further suggests the peculiarity of the sharp, asymmetric stress field and the uniqueness of the one-way cracking achieved working with TMMs.

2.2 Topological zero modes control asymmetric stress field

The strongly asymmetric distribution of stress induced by crack opening in TMMs can be understood via the analysis of the localized topological ZMs [44, 47, 48, 49, 50] that are triggered during the deformation process. Here we first discuss this effect in the case of ideal Maxwell lattices, featuring only nearest-neighbor (NN) bonds and then generalize it to structural TMMs featuring additional weak bending constraints which can be characterized by next-nearest-neighbor (NNN) bonds.

In a topological kagome lattice as a NN-bond only ideal Maxwell lattice, each node has 2 degrees of freedom from the in-plane displacements and 2 constraints from the 4 bonds connecting to it (as each bond is shared by 2 nodes). Maxwell's counting rule of equal numbers of degrees of freedom and constraints is satisfied at every wave number, and the system has two homogeneous ZMs (x, y translations) and two homogeneous SSSs that provides the elastic moduli. Assume removing one node in the bulk to open a small crack. This operation removes 2 degrees of freedom and 4 constraints, and as a result, it lifts the two homogeneous SSSs and creates 2 nearly-ZMs near the crack (Fig. 2A). The frequencies of these 2 nearly-ZMs vanish exponentially as a function of the system size. A simulation of the ideal lattice (under either periodic boundary conditions or fixed boundary conditions, if the lattice is large) reveals the spatial pattern of these two nearly-ZMs, which are localized around the right tip of the crack, as a result of the topological polarization $\mathbf{R}_{\mathrm{T}}$, following the predictions of topological mechanics theories [44, 47, 48]. The two nearly-ZMs are even $\mathbf{u}^{(e)}$ and odd $\mathbf{u}^{(o)}$ with respect to the horizontal mirror plane of the crack, respectively, and they have dynamical matrix eigenvalues λ_e, λ_o (corresponding to mode frequencies $\sqrt{\lambda_e/m}, \sqrt{\lambda_0/m}$ with m being the mass of the nodes). These two nearly-ZMs exhibit two supersymmetry partners, which are nearly-SSSs [44], $\mathbf{s}^{(e)}$ and $\mathbf{s}^{(o)}$.

The response of the lattice upon an external load of u_{yy} stretching, as we derive in detail in the SI II A, is dominated by the even nearly-ZM $\mathbf{u}^{(e)}$ (Fig. 2A) via

$$\mathbf{u}_i \simeq \mathbf{u}_i^{(\mathrm{aff})} - \frac{1}{\sqrt{\lambda_e}} \left(\sum_b \mathbf{s}_b^{(e)} \cdot \mathbf{E}_b^{(\mathrm{aff})} \right) \mathbf{u}_i^{(e)}, \tag{1}$$

where i labels the nodes, b labels the bonds, $\mathbf{u}^{(\mathrm{aff})}, \mathbf{E}^{(\mathrm{aff})}$ are the affine (homogeneous strain) displacement and bond extension of the lattice under the load, and the nonaffine response is controlled by the even nearly-ZM $\mathbf{u}_i^{(e)}$, with the coefficient given by the overlap of the affine strain $\mathbf{E}^{(\mathrm{aff})}$ with the corresponding even nearly-SSS $\mathbf{s}^{(e)}$.

A complimentary way to understand the topological nature of this strongly asymmetric displacement field is to realize that the bulk solution of ZMs in Maxwell lattices can be generally written in the form of $e^{i\mathbf{q}\cdot\mathbf{r}}$, where the imaginary part of $\mathbf{q}$ controls the decay of the ZMs [44, 52, 50]. The horizontal topological polarization $\mathbf{R_T}$ of the lattices we consider here directly controls the imaginary part of q_x of the ZMs. For each given real q_y, there are two ZM solutions, both of which have the imaginary part $q_x'' > 0$ for the topological kagome, but the two q_x''s have opposite signs for the twisted kagome which is unpolarized (Fig. S7). The actual displacement field upon loading comes from a linear combination of these ZMs, with the coefficients determined by the boundary conditions. The crack in the middle allows for finite displacement amplitude around it. The displacement must decay towards the right in the topological kagome, consistent with the numerical results (Fig. 2). Importantly, if there is any displacement amplitude on the left tip, it must exponentially increase towards the bulk on the left, which is not allowed. This requires vanishing displacement on the left tip in the topological ideal Maxwell lattice case. In contrast, in the twisted kagome lattice, decay occurs in both $\pm x$ directions, giving a ratio of displacements of order unity between the two tips (Fig. S7). This argument also generalizes this phenomenon from the one-node crack to other sizes and shapes of cut, as we mention below.

The discussions above describe the response of the NN-only topological Maxwell lattice under load, where due to the lack of SSSs, the lattice moves along the linear combination of the affine strain and the nonaffine nearly-ZM (Eq. (1)), and there is no stress to the linear order. The strong asymmetry of the nearly-ZM gives rise to the strong asymmetry of the displacement field of the lattice under load, leading to stress responses at the nonlinear level. To fully understand the stress response of the TMM, we theoretically analyze the topological kagome lattice with NNN bonds, and compare with numerical results on the NNN lattice characterized by a spring constant ratio $k_{\mathrm{NNN}}/k_{\mathrm{NN}}$, and the TMM which is a continuum model characterized by normalized hinge thickness $h/|\mathbf{a}_1|$. Firstly, we verify that despite the deviation from the ideal Maxwell limit, the displacement responses of the NNN lattice (Fig. 2B) and the TMM (Fig. 2C) under load is indeed dominated by the even nearly-ZM shown in Fig. 2A, featuring drastically different rotations at hinges at the left and right tips (Fig. 2D). Secondly, a subtle difference arises, as the weak additional constraints due to the NNN bonds or the bending stiffness of the hinges induce homogeneous SSSs even in presence of the crack. This leads to weak stress responses at the linear level, mainly carried by the NNN bonds (Fig. 2E). In contrast, the NN stress increases nonlinearly at small $k_{\mathrm{NNN}}/k_{\mathrm{NN}}$, as determined by the ideal theory. When the NNN spring constant or the hinge thickness becomes large, the lattice deviates from the ideal Maxwell case and crosses over to normal elastic media behavior where geometric details prevail, with the topological polarization effect vanishing (Fig. 2FG).

Due to the robustness of the topological polarization, this strong asymmetry of strain and stress applies more generally beyond this simple scenario of a small crack (Fig. S8). When the crack is longer, more nearly-ZMs are generated. However, due to the topological nature of the ZM profiles in the bulk, the excited combination of ZM is still characterized by strong stress on the right, as shown in Fig. 1, SI II B and Fig. S9. This also applies to holes of other shapes, as we discuss below. For simplicity, we will just use the term "ZMs" to refer to both exact ZMs and nearly-ZMs in other sections.

Furthermore, as the first hinge on the right breaks due to high stress, the lattice gains more ZMs which again asymmetrically localize more on the right than on the left due to the topological polarization $\mathbf{R}_{\mathrm{T}}$. The process of nonlinear deformation along the ZMs, generating high bending stress which evolves into stretching stress at higher strain at the right tip, occurs again until the next hinge breaks, and repeats until all hinges on the right break, as we show in Fig. 1. The nonlinear excitation of the topological ZMs is behind the ductility of this fracturing process, although the original material is brittle.

The results shown here are from periodic boundary conditions, so the topological mechanical effect at the crack is separated from the boundaries. We find that the topologically protected stress asymmetry is robust against the details of the boundary conditions. The results shown in Fig. 1 are from open boundary conditions, and we include more studies of boundary conditions in the SI II B.

2.3 Comparison with linear elastic fracture mechanics

It is instructive to compare the asymmetric stress fields observed in TMMs to the classical solution of linear elastic fracture mechanics (LEFM). In LEFM, the tip stress is symmetric between left and right tips, and the dependence of the tip stress field upon the angle around—and distance from—the crack tip can be treated as separated variables [61, 62, 63, 64]. Our tests and simulations suggest that the stress fields established in the Maxwell TMMs fundamentally differ from the LEFM cases in both respects. To quantitatively study this effect, we compare four cases: a topologically polarized kagome TMM, a regular kagome lattice, an elastic continuum, and the analytic solution from LEFM. For TMM and regular kagome, the stress fields are shown in Fig. 3A and B, respectively. Since most stress localizes at the hinges, here, for visualization purposes, we extract the hinge stresses (see Materials and Methods) and interpolate them over the entire sample domain to obtain a continuous effective stress field. The deviations from LEFM predictions can be agilely appreciated by inspection. The left-right symmetry is broken at the center of the tip, and this behavior is observed robustly for different values of the hinge thickness parameter h, as shown in Fig. 3E. Moreover, the angular stress dependence (profiles of stress vs. angle γ or $\widetilde{\gamma}$) is different when sampled at different distances (radii) from the tip, as shown in Fig. 3C, violating the independence of the radial and angular variables in LEFM. Fig. 3C also shows that the left and right tip stress fields feature qualitatively different angular dependence, revealing an additional element of asymmetry due to polarization. For completeness, an analogous study is given for the regular kagome (green curve) and for the continuum (dark gray curve with markers for numerical simulations and light gray curve for analytical solution) in Fig. 3D. Here, all the curves apply to all radii, as the dependence upon γ or $\widetilde{\gamma}$ is decoupled from that upon distance.

We further study the case of elliptical cracks in a continuum, for which finite LEFM analytic solutions are available, with emphasis on the dependence on the crack aspect ratio a/b. In Fig. 3F we show the stress field for a reference choice of a/b in a continuum. Not surprisingly, the stress field is symmetric close and far from the crack. From LEFM, the stress magnitude varies with a/b as $\sigma_{\mathrm{tip}} = \sigma_\infty(1+2a/b))$, where σ_∞ is the far-field stress [61, 62, 63, 64]. In Fig. 3G, we fix b and only vary a, de facto sweeping the aspect ratio between 1 and 4 and we monitor the ratio between the stress in the bulk, where the stress plateaus and can be taken as the far-field stress, and the tip stress. The trend of the gray curves confirm the expected decay. The slight deviation between simulation (dark gray with markers) and analytical solution (light gray) is due to numerics and progressively vanishes upon mesh refinement. In Fig. 3G we also repeat the analysis for the two considered lattices (TMM and regular kagome). Interestingly, here the tip-to-bulk stress ratio appears to be independent of a/b, with the usual asymmetry between left and right tip exhibited by the TMM. The independence on defect length implies special mechanical features of the TMM: compared to normal media, the metamaterial shows a larger fracture toughness with delayed cracking due to slower increase of stress focusing as crack size increases.

2.4 Topology-controlled fracture: a portfolio of patterns

The one-way fracture mechanism discussed above is not limited to straight line cracks located in the bulk. It also applies to initial cracks of different shapes or differently located in the lattice domain. This robustness attribute proceeds directly to the fact that the ZM-controlled fracture mechanism is topologically protected. We demonstrate this through three representative cases (schematically depicted and color-coded in Fig. 4A): (I) a tilted cut in the bulk (green), (II) a cut at the soft edge (blue), and (III) a cut at the rigid edge (orange). For (I), we first check the distribution of ZMs predicted by theory for the idealized NN lattice under periodic boundary conditions (similar to Fig. 2A). After removing sites and bonds along the direction of lattice vector $\mathbf{a_2}$ (Fig. 1B, Materials and Methods), all the ZMs are localized asymmetrically at only the right edge of the crack in Fig. 4B, as a result of topological polarization. We then examine the problem for the corresponding TMM in Fig. 4C. Simulations indicate that, under uniform stretching of the lattice, the deformation localizes at the right edge as well (see displacement color map in Fig. 4C). Consequently, the stress developed in the hinges on the right edge is greater than that at the left edge, as depicted in Fig.4D. A similar asymmetric pattern of ZMs and stress localization can also be found for other crack shapes (e.g., the triangular hole in Fig. S12).

To quantify this asymmetry, we define $\mathbf{n}$ as the vector normal to the crack edge and α the angle between $\mathbf{n}$ and the polarization vector $\mathbf{R}_{\mathrm{T}}$. It is known from theory of polarized Maxwell lattices that the density of ZMs at an edge is proportional to $\mathbf{n} \cdot \mathbf{R}_{\mathrm{T}} = \cos\alpha$ [44]. As described below, we find this quantity to be a good indicator of stress distribution around holes. In Fig. 4E, we consider holes of different orientations and plot the magnitude of ZMs at the edge and the bulk-to-edge stress ratio against the angle α. When α approaches π (or $\cos\alpha \to -1$), the edge has no localized ZMs (the left side of the crack in Fig. 2A, Fig. 4B) and shows the same hinge stress as the bulk stress (Fig. 3A). On the other hand, as α goes to 0, the stress ratio approaches 0, implying a significant stress concentration at the edge. Here, the hinge thickness is set to $h/|\mathbf{a_1}| = 0.015$ in Fig. 4C-E.

This asymmetry of stress distribution leads to robustly controllable crack propagation directions for a variety of hole orientations occurring in TMM domains, which we demonstrate numerically and experimentally in Fig. 4F, G. The initial state has a crack along $\mathbf{a_2}$ in Fig. 4F. After being stretched, both nonlinear simulations and experiments show that the crack initially propagates to the right, emanating from the bottom-right tip and breaking sequentially the two adjacent hinges (Fig. 2G). After that, the crack also propagates to the left side, as shown in the Movie S5, likely due to the proximity of the crack to the right boundary. The results emphasize that the unidirectional cracking mechanism is invariant to the shape of the bulk crack (see one-way cracking of a triangle notch in Movie S6 and a rectangular notch in Movie S7).

The same principle also controls stress fields and crack propagation driven by edge cuts, with some noteworthy differences between soft (cases II) and rigid (cases III) edges. In Fig. 4H, via simulations we calculate and plot the stress developed along the hinges in the same row along which the crack propagates, from the crack tip to the other side of the sample. We observe qualitatively different trends between the two cases. When the initial crack is at the soft edge, the stress drops sharply into the bulk, whereas when the initial crack is at the rigid edge, the stress decreases gradually. Overall, the decay of the soft edge curve follows a trend similar to the decay of hinge stress along the right tip path observed for the bulk crack in Fig. 3C. As shown in the experiment with initial crack at the soft edge (Fig. 4I-J), since the tip hinge has a much larger stress than the surrounding hinges (Fig. 4I inset), the crack *always* propagates along the straight path (Fig. 4J). In contrast, the stress at the rigid edge is diffusive, uniformly distributed around the tip, as indicated by the color of the dots in the K inset (consistent with the numerical prediction in Fig. 4H). This results in *multiple potential crack paths*, as observed in the experiments documented in Fig. 4K-M. As a result, small random perturbations caused by experimental non-idealities can cause unexpected bifurcations of the cracking paths. In Fig. 4L, the crack turns directly into the direction along $\mathbf{a_2}$. In the case shown Fig. 4M, the crack propagates straightly first and then turns into the direction along $\mathbf{a_2}$ at a later stage. Furthermore, in both simulations and experiments, the rigid edge exhibits delayed cracking compared to the soft edge (Fig. S15E, F), despite similar force peaks in the force-displacement curves for cases (II) and (III).

These differences in fracturing behavior between the two edges suggest that crack tips in TMM display a variety of regimes, ranging from stable propagation at the soft tip to diffusive cracking at the rigid tip. Diffusive failures, characterized by fracturing without stress concentration, typically occur in systems with high disorder or low connectivity [69, 25, 24] Previously, people achieve concentrated stress and diffusive stress tips in different systems by tuning network connectivity [70] or rigidity [9, 25, 24]. The former appears in highly connected or rigid systems, while the latter shows up in systems with low connectivity. Here, we demonstrate that both concentrated and diffusive stress can emerge within the same over-constrained real system, allowing for on-demand fracturing control.

3 Conclusions and discussions

Using a combination of theory, computations, and experiments, we have shown that Maxwell-lattice based TMMs are capable of guiding fracture in a unidirectional way, achieving ductile failure even when the constituent material is brittle. The directionality is predictable as a result of the topological protection of the polarization, which overwhelms the randomness associated with experimental variability. The ability to customize stress fields around crack tips offers a robust yet versatile set of tools to design light-weight, material- and scale-invariant metamaterials with on-demand fracture control. The phenomena observed at the lattice scale fundamentally deviate from the classical theory of LEFM (which however still govern the elasticity of the problem at the smaller scale of the structural constituents of the lattice, e.g., the individual hinges) in multiple aspects, including the asymmetry of stress fields across the crack and the strong angular dependence of the spatial decay rate of stress. These unique properties can be exploited to design strategies to control or engineer failure mechanisms and patterns, as conceptually put forth in this manuscript.

We have provided a rationale for the observed one-way fracture using topological mechanics theory, pinpointing the phenomenon to topologically protected ZMs that arise in Maxwell lattice TMMs: essentially, external loads excite ZMs which localize at the crack tips carrying the asymmetry signature of the lattice polarization, leading to anisotropic stress fields around cracks and thus an anisotropic landscape of drivers of crack propagation. Because ZMs in TMMs are controlled by the bulk topology of the phonon structure (notwithstanding the dilution occurring in the structural lattice, see remark below), their directional localization is robust and independent of specific geometrical features of the lattice. In addition, similar to other recent experimental demonstrations of TMMs, the topological effects are the most prominent when the system is close to the ideal Maxwell limit where bending stiffness at the hinges are low. As the hinges become thicker, the topological polarization and its effect on controlling crack propagation is progressively diluted.

Furthermore, the full potential of topological mechanics in realistic experimental systems and applications in engineering is far from understood. In particular, the requirement of "thin hinges" to realize Maxwell lattice topological mechanics has been a challenge for both fabrication and durability of these TMMs. Experiments presented in this paper offers a new perspective of an easy, efficient, kirigami-like approach to fabricate the TMMs, as well as providing strategies to protect the integrity of potentially delicate TMMs from catastrophic failures.

The directional fracture phenomenon discussed in this paper opens a new approach for controlling sequences and directions of crack propagation, demonstrating great potential for broad applications beyond the specific problem discussed here and across scales. While non-topological structures are sensitive to both arbitrary and systematic changes in their micro-geometries, TMMs exhibit topologically protected properties that are independent of scale or material. For instance, at the micro-scale, topologically engineered mechanical frames have been integrated with the self-assembly of nanoparticles [71]. Thus, with an appropriate design, the fracturing control strategies developed for TMMs can also be applied to manage nanoparticle interactions and pattern formation at the micro-scale. At the larger scale, truss and tensegrity structures have started to be an integral part of the design of buildings and aircraft [72]. The availability of predictable and ductile cracking process can be a powerful attribute for the safety of those structures.

Materials and Methods

Experiments

We utilize Silhouette Cameo 4 Cutting Machine for cutting all the experiment samples. Our blade is the 0.2 mm Kraft Blade. We ensure that none of the hinges are broken before loading, to minimize initial imperfections. For the photo elastic setup in Fig. 1C and Fig. S2, we set one polarizer in the front of the sample and the other behind the sample (with a 90 deg angle difference of the transmitting axis of the front one). The photo elastic thin film is Polyethylenimine (PEI) film with a thickness of 0.076 mm, purchased from McMASTER-CARR. The loading is performed quasi-statically, with a speed of 2 mm per minute. In Fig. 1, sample width $w = 152.4$ mm, sample length $L = 157$ mm, crack length $2a = 75$ mm, and hinge thickness $h \approx 0.8$ mm ($h/|\mathbf{a_1}| = 0.06$) in Fig. 1H-L and Fig. 4F, G, I-M.

In Fig. 1(D-M) and Fig. 4, the cardboard paper is the Wexford Folder 2-pocket (0.26 mm thick), purchased from Walgreens. Each paper sample weighs 3.6 g. The loading machine is Instron 4301 equipped with a 100 N loading cell and a 10 kN load cell. To allow uniform stretching/clamping at the top/bottom boundaries, we prepare four aluminum pieces (1.6 mm thick), sandwich each of the two sides between two pieces and glue them together. In Fig. 1D, for each of the three geometries, ten samples are loaded to observe the probabilities of fracturing direction.

In the material test, the strip samples have the size of 70 mm by 30 mm. Paper has two main axes (Fig. [73]), and in this work all the experimental stretching is along the length direction. In Fig. S2D, the long edge of the strip is cut along the length direction of the paper folder.

Simulations

We use finite element software Abaqus/CAE 2023 for simulations [74]. Since we utilize cardboard paper as brittle material in experiments, we experimentally measured its stress-strain curve (Fig. S2D, Fig. S16A), and input that as the material parameters in the simulations. For spring-mass lattices, we apply truss elements (T2D3), which have no bending stiffness and can only carry axial stress. For continuous geometries, we choose reduced shell element (S4R).

We perform three types of simulations, linear frequency analysis (mode analysis in Fig. 2A, Fig. 4B), implicit static analysis (linear stress distribution in Fig. 1C, Fig. 2B, C, Fig. 3, and Fig. 4 C-E, H, inset of I, K) and explicit cracking simulations (Fig. 1 and Fig. 4G). For periodic boundary conditions (along x) in Fig. 2 and Fig. 4, we couple the degree of freedom of the left boundaries nodes with that of the right boundary nodes. The ZM weight is obtained via $U_i \equiv \sqrt{\sum_{\mathrm{ZM}} \mathbf{u_i}^2}$, where i labels the nodes [75]. In explicit cracking simulations, we allow element deletion and strain failure criteria. For simplification and better visualization, the stress fields are normalized by comparing the stress to the largest stress in the system in Fig. 1A, H-L, Fig. 2C, Fig. 4. In all simulation results, the stress magnitude before normalization is between 0 and 7×10^7 Pa (Fig. S16). In Fig. 1C, to compare the differences in stress distribution, we apply the displacement in the simulations, and then normalize the sum of extracted stresses in the three geometries to ensure that they exhibit the same total reaction stress.

For the implicit static analyses in Fig. 1C, Fig. 2G, Fig. 3 and Fig. 4E, H, I, K, we obtain a single value of stress out of a hinge with finite width. Since the stresses are concentrated at the hinges, we distribute extra fine meshes at all the hinges. For each hinge, we average the stresses over the elements at its thinnest cross-section (Fig. S4).

Code availability

The codes that support the findings of this study are available on the public repository Github.

Acknowledgments

This work is supported by the National Science Foundation CMMI-2026794 (X.W, and X.M.) and CMMI-202700 (S.G.) and by the Office of Naval Research MURI N00014-20-1-2479 (X.W., S.S., and X.M.). We thank Fan Liu, Qi Zhang, Shi-Qing Wang, Mohammad Charara, Kai Sun, and Nick Kotov for fruitful discussions. We thank Andy Poli and Ellen Arruda's lab for their great help in setting up the experiments. We are grateful to the Advanced Research Computing at University of Michigan for access to the software and computational resources used in the simulations.

Author Contributions

All the authors designed the project. S.S., X.M. and X.W. conducted theoretical derivation. X.W. and S.S. performed numerical simulations. X.W. conducted experiments. All the authors analyzed the data, wrote and improved the manuscript.

References

[1] Allegre CJ, Le Mouel J, Provost A. Scaling rules in rock fracture and possible implications for earthquake prediction. Nature. 1982;297(5861):47-9.

[2] Peterlik H, Roschger P, Klaushofer K, Fratzl P. From brittle to ductile fracture of bone. Nature materials. 2006;5(1):52-5.

[3] Chai H, Lee JJW, Constantino PJ, Lucas PW, Lawn BR. Remarkable resilience of teeth. Proceedings of the National Academy of Sciences. 2009;106(18):7289-93.

[4] Shen T, Song Z, Cai S, Vernerey FJ. Nonsteady fracture of transient networks: The case of vitrimer. Proceedings of the National Academy of Sciences. 2021;118(29):e2105974118.

[5] Tang J, Li J, Vlassak JJ, Suo Z. Fatigue fracture of hydrogels. Extreme Mechanics Letters. 2017;10:24-31.

[6] Li X, Cui K, Sun TL, Meng L, Yu C, Li L, et al. Mesoscale bicontinuous networks in self-healing hydrogels delay fatigue fracture. Proceedings of the National Academy of Sciences. 2020;117(14):7606-12.

[7] Barney CW, Ye Z, Sacligil I, McLeod KR, Zhang H, Tew GN, et al. Fracture of model end-linked networks. Proceedings of the National Academy of Sciences. 2022;119(7):e2112389119.

[8] Lin S, Liu X, Liu J, Yuk H, Loh HC, Parada GA, et al. Anti-fatigue-fracture hydrogels. Science advances. 2019;5(1):eaau8528.

[9] Berthier E, Kollmer JE, Henkes SE, Liu K, Schwarz JM, Daniels KE. Rigidity percolation control of the brittle-ductile transition in disordered networks. Physical Review Materials. 2019;3(7):075602.

[10] Fan Z, Wang SQ. Resolving stress state at crack tip to elucidate nature of elastomeric fracture. Extreme Mechanics Letters. 2023;61:101986.

[11] Slootman J, Waltz V, Yeh CJ, Baumann C, Göstl R, Comtet J, et al. Quantifying rate-and temperature-dependent molecular damage in elastomer fracture. Physical Review X. 2020;10(4):041045.

[12] Chen S, Ravi-Chandar K. Nonlinear poroviscoelastic behavior of gelatin-based hydrogel. Journal of the Mechanics and Physics of Solids. 2022;158:104650.

[13] Yang Y, Song Z, Lu G, Zhang Q, Zhang B, Ni B, et al. Intrinsic toughening and stable crack propagation in hexagonal boron nitride. Nature. 2021;594(7861):57-61.

[14] Zhang X, Nguyen H, Zhang X, Ajayan PM, Wen J, Espinosa HD. Atomistic measurement and modeling of intrinsic fracture toughness of two-dimensional materials. Proceedings of the National Academy of Sciences. 2022;119(45):e2206756119.

[15] Lew AJ, Yu CH, Hsu YC, Buehler MJ. Deep learning model to predict fracture mechanisms of graphene. npj 2D Materials and Applications. 2021;5(1):48.

[16] Odde DJ, Ma L, Briggs AH, DeMarco A, Kirschner MW. Microtubule bending and breaking in living fibroblast cells. Journal of cell science. 1999;112(19):3283-8.

[17] Morley CD, Ellison ST, Bhattacharjee T, O'Bryan CS, Zhang Y, Smith KF, et al. Quantitative characterization of 3D bioprinted structural elements under cell generated forces. Nature communications. 2019;10(1):3029.

[18] Long R, Hui CY, Gong JP, Bouchbinder E. The fracture of highly deformable soft materials: A tale of two length scales. Annual Review of Condensed Matter Physics. 2021;12(1):71-94.

[19] Font-Clos F, Zanchi M, Hiemer S, Bonfanti S, Guerra R, Zaiser M, et al. Predicting the failure of two-dimensional silica glasses. Nature communications. 2022;13(1):2820.

[20] Deng B, Wang S, Hartquist C, Zhao X. Nonlocal intrinsic fracture energy of polymerlike networks. Physical Review Letters. 2023;131(22):228102.

[21] Kammer DS, McLaskey GC, Abercrombie RE, Ampuero JP, Cattania C, Cocco M, et al. Earthquake energy dissipation in a fracture mechanics framework. Nature communications. 2024;15(1):4736.

[22] Heisser RH, Patil VP, Stoop N, Villermaux E, Dunkel J. Controlling fracture cascades through twisting and quenching. Proceedings of the National Academy of Sciences. 2018;115(35):8665-70.

[23] Fuentealba JF, Hamm E, Roman B. Intertwined multiple spiral fracture in perforated sheets. Physical Review Letters. 2016;116(16):165501.

[24] Zhang L, Rocklin DZ, Sander LM, Mao X. Fiber networks below the isostatic point: Fracture without stress concentration. Physical Review Materials. 2017;1(5):052602.

[25] Driscoll MM, Chen BGg, Beuman TH, Ulrich S, Nagel SR, Vitelli V. The role of rigidity in controlling material failure. Proceedings of the National Academy of Sciences. 2016;113(39):10813-7.

[26] Ma X, Wei Y. Programming fracture patterns of thin films. Physical Review E. 2022;105(2):025002.

[27] Wang M, Shi S, Fineberg J. Tensile cracks can shatter classical speed limits. Science. 2023;381(6656):415-9.

[28] Pons AJ, Karma A. Helical crack-front instability in mixed-mode fracture. Nature. 2010;464(7285):85-9.

[29] Vandenberghe N, Vermorel R, Villermaux E. Star-shaped crack pattern of broken windows. Physical review letters. 2013;110(17):174302.

[30] Marthelot J, Roman B, Bico J, Teisseire J, Dalmas D, Melo F. Self-replicating cracks: a collaborative fracture mode in thin films. Physical review letters. 2014;113(8):085502.

[31] Takei A, Roman B, Bico J, Hamm E, Melo F. Forbidden directions for the fracture of thin anisotropic sheets: an analogy with the wulff plot. Physical review letters. 2013;110(14):144301.

[32] Bailey NP, Sethna JP. Macroscopic measure of the cohesive length scale: Fracture of notched single-crystal silicon. Physical Review B. 2003;68(20):205204.

[33] Hamm E, Sivak I, Roman B. Nature of Crack Path Instabilities in Thin Sheets Cut by Blunt Objects. Physical review letters. 2020;124(17):174101.

[34] Fuentealba JF, Marthelot J, Roman B, Melo F. Collaborative Oscillatory Fracture. Physical Review Letters. 2020;124(17):174102.

[35] Martins AF, Bennett NC, Clavel S, Groenewald H, Hensman S, Hoby S, et al. Locally-curved geometry generates bending cracks in the African elephant skin. Nature communications. 2018;9(1):1-8.

[36] Barthelat F, Tang H, Zavattieri P, Li CM, Espinosa H. On the mechanics of mother-of-pearl: a key feature in the material hierarchical structure. Journal of the Mechanics and Physics of Solids. 2007;55(2):306-37.

[37] Lew AJ, Stifler CA, Tits A, Schmidt CA, Scholl A, Cantamessa A, et al. A Molecular-Scale Understanding of Misorientation Toughening in Corals and Seashells. Advanced Materials. 2023;35(28):2300373.

[38] Domino L, d'Augères MB, Zhang J, Janbaz S, Aragòn AM, Coulais C. Fracture metamaterials with on-demand crack paths enabled by bending. arXiv preprint arXiv:240519061. 2024.

[39] Brodnik N, Brach S, Long C, Ravichandran G, Bourdin B, Faber K, et al. Fracture diodes: Directional asymmetry of fracture toughness. Physical Review Letters. 2021;126(2):025503.

[40] Souto A, Zhang J, Aragón AM, Velikov KP, Coulais C. Edible mechanical metamaterials with designed fracture for mouthfeel control. Soft Matter. 2022;18(15):2910-9.

[41] Mirkhalaf M, Dastjerdi AK, Barthelat F. Overcoming the brittleness of glass through bio-inspiration and micro-architecture. Nature communications. 2014;5(1):3166.

[42] Noah PM, Koning V, Vitelli V, Irvine WTM. Fracture in sheets draped on curved surfaces. Nature Materials. 2017;16:89-93.

[43] Klein Y, Sharon E. Buckling-fracture transition and the geometrical charge of a crack. Physical Review Letters. 2021;127(10):105501.

[44] Kane CL, Lubensky TC. Topological boundary modes in isostatic lattices. Nature Physics. 2014;10(1):39-45.

[45] Wang P, Lu L, Bertoldi K. Topological phononic crystals with one-way elastic edge waves. Physical review letters. 2015;115(10):104302.

[46] Nash LM, Kleckner D, Read A, Vitelli V, Turner AM, Irvine WT. Topological mechanics of gyroscopic metamaterials. Proceedings of the National Academy of Sciences. 2015;112(47):14495-500.

[47] Lubensky T, Kane C, Mao X, Souslov A, Sun K. Phonons and elasticity in critically coordinated lattices. Reports on Progress in Physics. 2015;78(7):073901.

[48] Mao X, Lubensky TC. Maxwell lattices and topological mechanics. Annual Review of Condensed Matter Physics. 2018;9(1):413-33.

[49] Zhou D, Zhang L, Mao X. Topological edge floppy modes in disordered fiber networks. Physical review letters. 2018;120(6):068003.

[50] Sun K, Mao X. Continuum theory for topological edge soft modes. Physical Review Letters. 2020;124(20):207601.

[51] Cheng W, Qian K, Cheng N, Boechler N, Mao X, Sun K. Backscattering-free edge states below all bands in two-dimensional auxetic media. arXiv preprint arXiv:230607493. 2023.

[52] Rocklin DZ, Zhou S, Sun K, Mao X. Transformable topological mechanical metamaterials. Nature communications. 2017;8(1):14201.

[53] Xiu H, Liu H, Poli A, Wan G, Sun K, Arruda EM, et al. Topological transformability and reprogrammability of multistable mechanical metamaterials. Proceedings of the National Academy of Sciences. 2022;119(52):e2211725119.

[54] Jolly JC, Jin B, Jin L, Lee Y, Xie T, Gonella S, et al. Soft mechanical metamaterials with transformable topology protected by stress caching. Advanced Science. 2023;10(22):2302475.

[55] Paulose J, Meeussen AS, Vitelli V. Selective buckling via states of self-stress in topological metamaterials. Proceedings of the National Academy of Sciences. 2015;112(25):7639-44.

[56] Zhang L, Mao X. Fracturing of topological Maxwell lattices. New Journal of Physics. 2018;20(6):063034.

[57] Widstrand C, Hu C, Mao X, Labuz J, Gonella S. Stress focusing and damage protection in topological Maxwell metamaterials. International Journal of Solids and Structures. 2023;274:112268.

[58] Widstrand C, Mao X, Gonella S. Robustness of stress focusing in soft lattices under topology-switching deformation. Extreme Mechanics Letters. 2024;68:102135.

[59] Ma J, Zhou D, Sun K, Mao X, Gonella S. Edge modes and asymmetric wave transport in topological lattices: Experimental characterization at finite frequencies. Physical review letters. 2018;121(9):094301.

[60] Charara M, McInerney J, Sun K, Mao X, Gonella S. Omnimodal topological polarization of bilayer networks: Analysis in the Maxwell limit and experiments on a 3D-printed prototype. Proceedings of the National Academy of Sciences. 2022;119(40):e2208051119.

[61] Griffith AA. VI. The phenomena of rupture and flow in solids. Philosophical Transactions of the Royal Society of London. 1921;221(582-593):163-98.

[62] Lawn B. Fracture of brittle solids. Cambridge university press; 1993.

[63] Inglis C. Stresses in a plate due to the presence of cracks and sharp corners. Transactions of the Institute of Naval Architects. 1913;55:219-41.

[64] Zehnder AT. Lecture notes on fracture mechanics. Cornell University. 2007;20:22.

[65] Charara M, Sun K, Mao X, Gonella S. Topological flexural modes in polarized bilayer lattices. Physical Review Applied. 2021;16(6):064011.

[66] Janssen M, Zuidema J, Wanhill R. Fracture mechanics: fundamentals and applications. CRC Press; 2004.

[67] Fleck NA, Qiu X. The damage tolerance of elastic–brittle, two-dimensional isotropic lattices. Journal of the Mechanics and Physics of Solids. 2007;55(3):562-88.

[68] Jia Z, Liu F, Jiang X, Wang L. Engineering lattice metamaterials for extreme property, programmability, and multifunctionality. Journal of Applied Physics. 2020;127(15).

[69] Shekhawat A, Zapperi S, Sethna JP. From damage percolation to crack nucleation through finite size criticality. Physical review letters. 2013;110(18):185505.

[70] Bouzid M, Del Gado E. Network topology in soft gels: Hardening and softening materials. Langmuir. 2018;34(3):773-81.

[71] Qian C, Stanifer E, Ma Z, Luo B, Liu C, Yao L, et al. Nanoscale Imaging of Phonons and Reconfiguration in Topologically-Engineered, Self-Assembled Nanoparticle Lattice. arXiv preprint arXiv:240315627. 2024.

[72] Liu K, Zegard T, Pratapa PP, Paulino GH. Unraveling tensegrity tessellations for metamaterials with tunable stiffness and bandgaps. Journal of the Mechanics and Physics of Solids. 2019;131:147-66.

[73] Wang X, Guest SD, Kamien RD. Keeping it together: interleaved kirigami extension assembly. Physical Review X. 2020;10(1):011013.

[74] Abaqus Analysis User's Manual (Dassault Systems, 2017);.

[75] Zhou D, Zhang L, Mao X. Topological boundary floppy modes in quasicrystals. Physical Review X. 2019;9(2):021054.

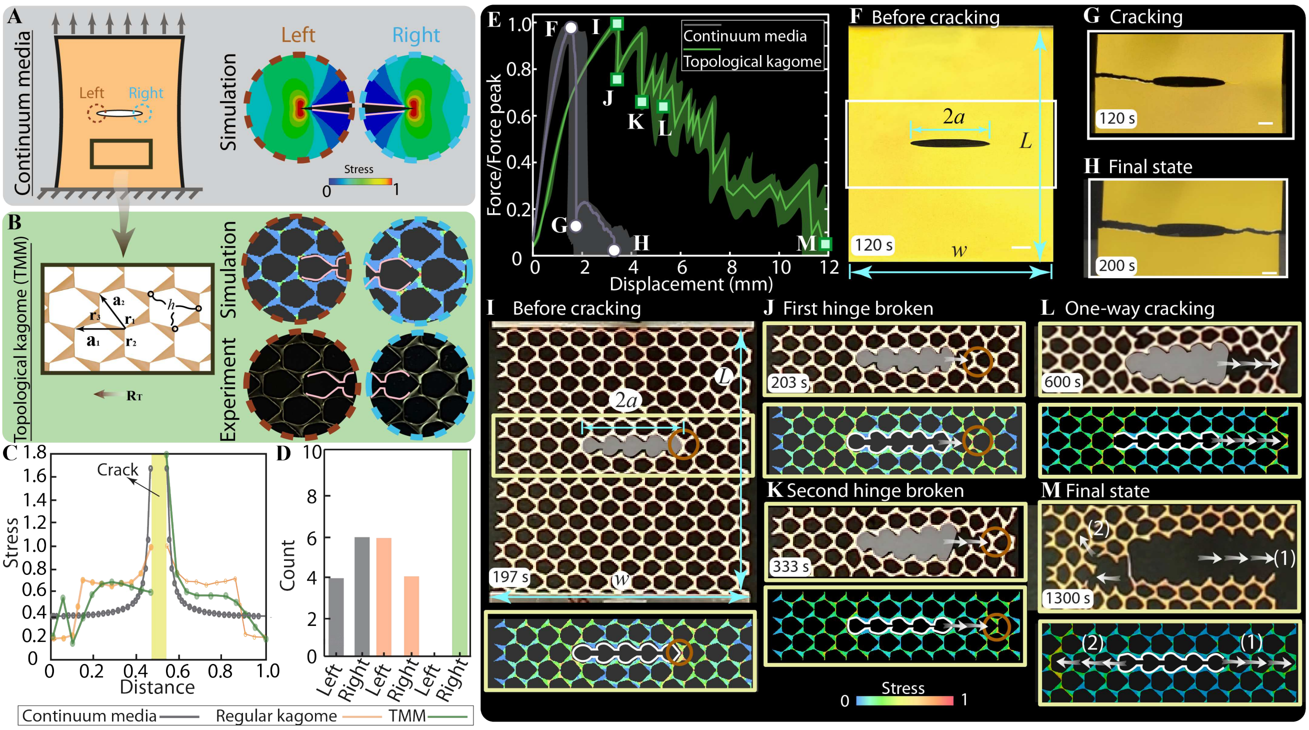

Figure 1: Unlike unpredictable failures seen in usual brittle materials, Maxwell TMMs exhibit robust and ductile one-way fracturing. (A) Classical fracturing: a symmetric stress field is generated by stretching an isotropic, homogeneous media with a crack. Inset: stress field at the two tips in simulations. Pink lines indicate the crack. (B) Stress field of a Maxwell TMM with primitive lattice vectors $\mathbf{a}_1 = (-3.1436, 0)$ and $\mathbf{a}_2 = (-1.5718, 2.1760)$. The positions of the lattice sites inside one unit cell of the lattices are $\mathbf{r}_1 = (0.0318, 0.896)$, $\mathbf{r}_2 = (0, 0)$ and $\mathbf{r}_3 = (-1.54, 1.28)$. h is the thickness of hinges. $\mathbf{R_T}$ is the topological polarization vector. Inset (upper): stress field at the two tips (simulation). Inset (lower): photoelastic stress images at the two tips (experiments). Brighter areas carry larger stress. Pink lines indicate the crack. (C) Stress profile across the system along the horizontal paths including the crack in continuum media, regular kagome, and TMM. Their geometries are shown in Fig. S3. (D) The count of crack propagation to the left and to the right in continuum media, TMM and regular kagome, out of 10 experiments in each case. (E) The dependence of normalized force (force/peak force) on displacements (unit: mm) in experiments. (F-H) Image sequence of a stretched continuum sample in the experiment, including (F) the peak state before cracking, (G) the catastrophic drop, and (H) the failed state of the continuum sample in the experiment. $2a$ is the length of the crack. w and L are the width and length of the sample, respectively. (I-M) Image sequence of stretching the TMM in both experiments (upper) and simulations (lower), including (I) the peak state before cracking, (J) after the first crack, (K) after the second crack, (L) after breaking all hinges on the right side (except the special last one) and (M) final state of the TMM. The units in thick brown circles undergo a lot more deformation than others, indicating cracks. All the stress shown here is von Mises stress. Scale bar: 12.5 mm.

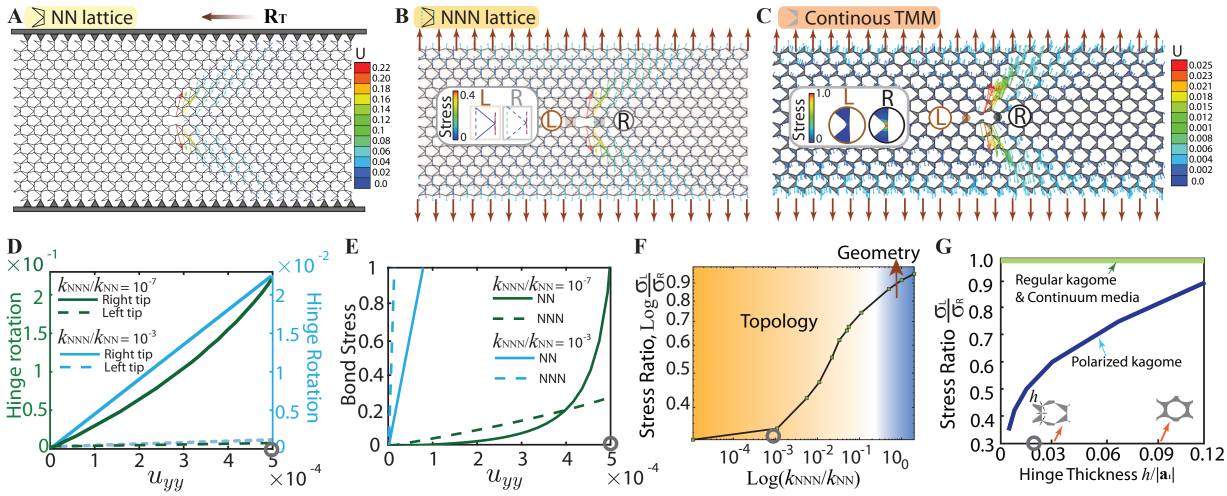

Figure 2: Topological ZMs explain the asymmetric stress field. (A) The topological even nearly-ZM $\mathbf{u}^{(e)}$ of the NN spring-mass lattice, which is an ideal Maxwell lattice. Being stretched to $u_{yy} = 5 \times 10^{-4}$ (strain, defined as the external displacement over the original sample length), the displacement field of (B) the next nearest neighbor (NNN) lattice ($k_{\mathrm{NNN}}/k_{\mathrm{NN}} = 10^{-3}$) and (C) the continuous TMM ($h/|\mathbf{a_1}| = 0.015$) closely resemble the nearly-ZM in (A), verifying that the asymmetry in the displacement and stress is due to the topological nearly-ZM. Inset: normalized von Mises stress of the two hinges at the tip. For better visualization, the NNN bonds are either hidden or dashed. (D) The dependence of tip hinge rotation angle (in radian) on the global strain u_{yy}, at different $k_{\mathrm{NNN}}/k_{\mathrm{NN}}$ ratios. (E) The bond stress (in the right tip unit) as a function of u_{yy}, when $k_{\mathrm{NNN}}/k_{\mathrm{NN}} = 10^{-7}$ and $= 10^{-3}$. The stress is normalized by the largest stress in the NN bond when $k_{\mathrm{NNN}}/k_{\mathrm{NN}} = 10^{-7}$. (F) The dependence of the stress ratio (the left to the right unit at the crack) on the bond stiffness ratio $k_{\mathrm{NNN}}/k_{\mathrm{NN}}$. When $k_{\mathrm{NNN}}/k_{\mathrm{NN}}$ is small, the left-to-right ratio is controlled by topology and as $k_{\mathrm{NNN}}/k_{\mathrm{NN}}$ increases, the topological mechanical effects dilute and the left-to-right ratio becomes the effect of geometric details. (G) The dependence of the stress ratio (left tip hinge to right tip hinge) on the hinge thickness in continuous geometries (von Mises stress). The gray circle on the x axis in (D-F) and (G) present the state in (B) and (C), respectively.

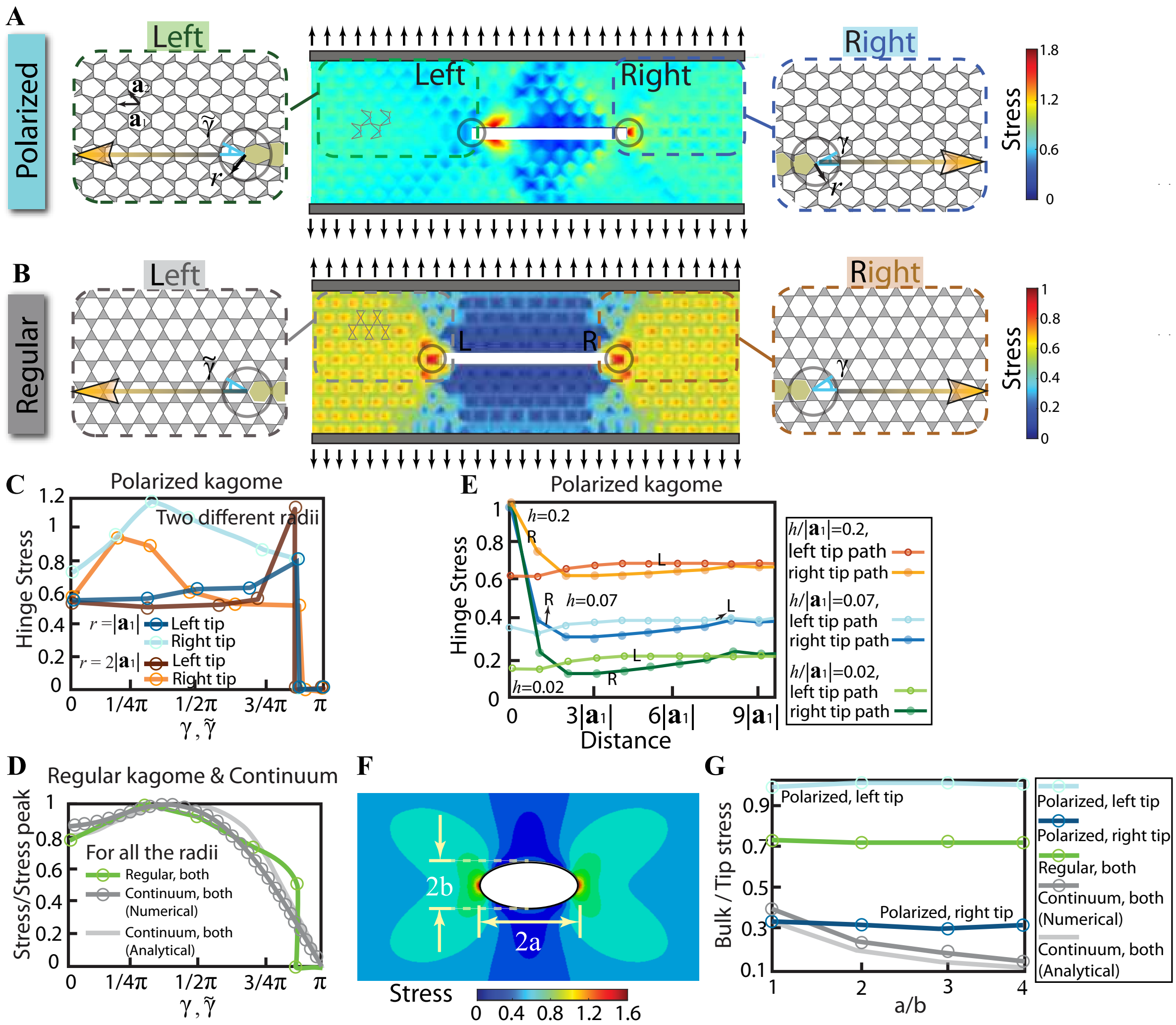

Figure 3: Comparison of the stress distribution in a topologically polarized kagome TMM and a regular kagome lattice (PBC along x) with linear elastic fracture mechanics (LEFM). Coarse-grained stress field (von Mises stress) of (A) polarized kagome TMM and (B) regular kagome under uniform stretching. Hinge thickness is $h/|\mathbf{a_1}| = 0.015$. Insets are details of the lattice geometries and paths of the boxed regions. γ and $\tilde{\gamma}$ are the angles from the horizontal direction. r is the distance from the crack tip. Orange arrows in the lattices indicate the paths from crack tip to the bulk. (C) The angular variation of the hinge stress of both left and right tip in the polarized kagome, for two different small radius r, $r = |\mathbf{a}_1|$ and $r = 2|\mathbf{a}_1|$. (D) The angular variation of hinge stress of both tips in the regular kagome and continuum, for all the small radius r. (E) The dependence of hinge stress on the hinge thickness along the left path and right path in (A). The hinge thicknesses of the three cases are $h/|\mathbf{a_1}| = 0.02$, 0.07, and 0.2, respectively. The stress in each of the three cases is normalized to the largest stress in the corresponding case. (F) Simulated stress field of an elliptical crack in the continuum media. (G) Bulk-to-tip stress ratio plotted against the aspect ratio a/b of the crack. We use von Mises stress in this figure. In the simulations, crack length $2a$ is varied while crack height $2b$ is fixed. The bulk stress is measured at a distance of $5a$ from the tip.

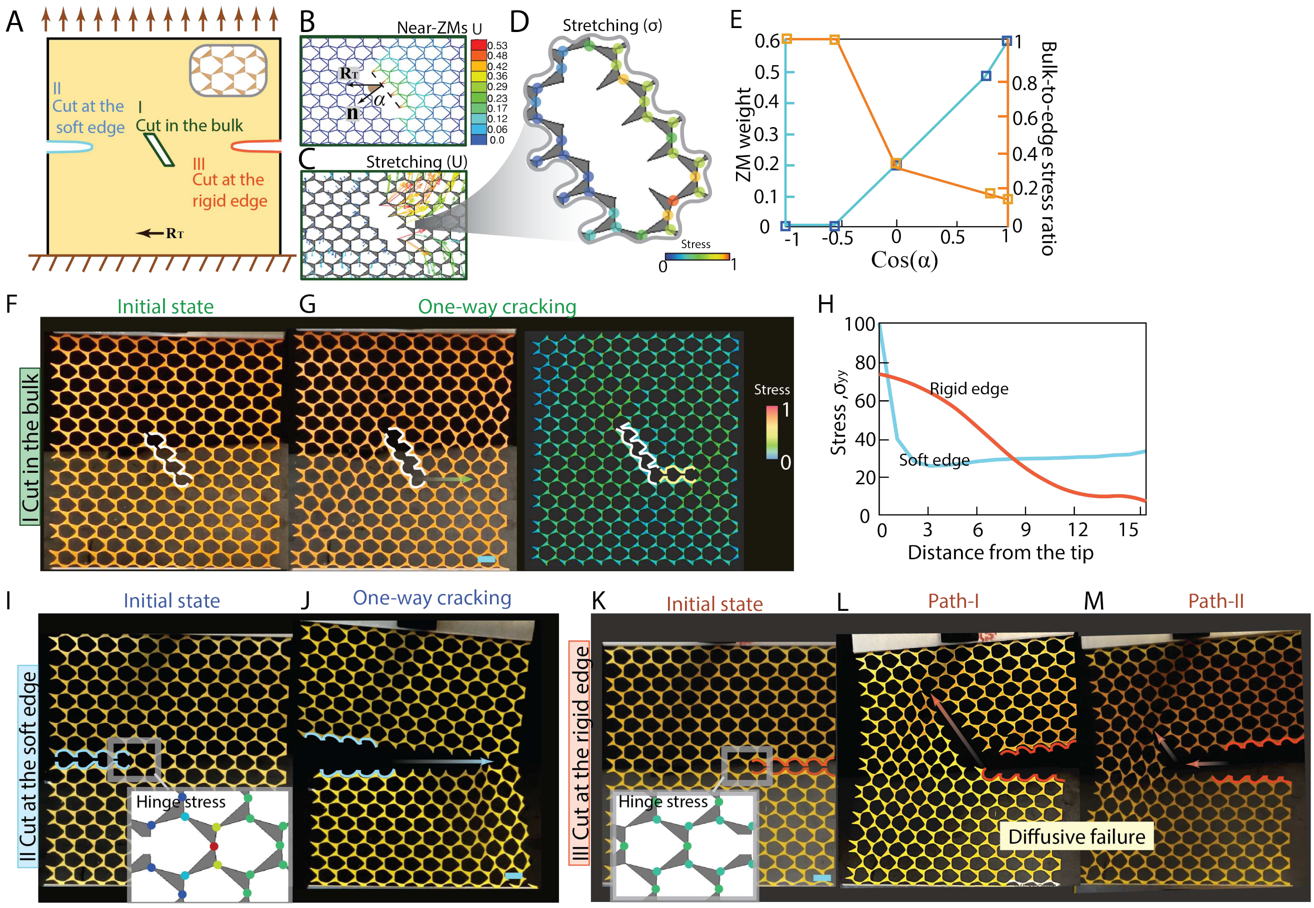

Figure 4: Analysis of three kinds of cuts in the TMM. (A) Schematic of (I) the cut in the bulk, (II) the cut at the soft edge, and (III) the cut at the rigid edge. (B) ZM weight U [75] in the topological kagome lattice with a tilted cut along $\mathbf{a_2}$. α is the angle between the cut edge normal $\mathbf{n}$ and $\mathbf{R}_\mathrm{T}$. Stretching the corresponding continuous TMM, we see (C) the displacement field and (D) hinge stress near the crack (normalized von Mises stress) are controlled by the topological ZMs in the spring-mass model. The stress of each individual hinge is indicated by the color of the dots. (E) Dependence of the magnitude of ZMs and bulk-to-edge stress ratio on the angle α. With an initial notch along the lattice vector $\mathbf{a_2}$, (F) the initial state in the experiment and (G) the unidirectional cracking phenomena in both experiment and simulation (normalized von Mises stress) after stretching. (H) The elastic stress response of the hinges along the row of the crack for two edge cracks in simulations. $x = 0$ and $x = 16$ refer to the crack tip and the other free edge, respectively. (I) Initial state of the geometry with the cut at the soft edge. Inset: hinge stress near the tip. The stress of each individual hinge is indicated by the color of dots. (J) Stable one-way cracking path after stretching. (K) Initial state of the geometry with the cut at the rigid edge. Inset: hinge stress near the tip. The stress of each individual hinge is indicated by the color of dots. (L) Path-I cracking and (M) Path-II cracking upon stretching. Hinge thickness is set to $h/|\mathbf{a_1}| = 0.015$ in (C-E). Scale bar: 12.5 mm.

Supplementary Files

This is a list of supplementary files associated with this preprint. Click to download.

- SI.pdf